



## Diagnostic Characterization of High Power Lithium-Ion Batteries for Use in Hybrid Electric Vehicles

X. Zhang,<sup>a,\*</sup> P. N. Ross, Jr.,<sup>a,\*</sup> R. Kostecki,<sup>b,\*</sup> F. Kong,<sup>b</sup> S. Sloop,<sup>b</sup> J. B. Kerr,<sup>b,\*</sup>  
K. Striebel,<sup>b,\*</sup> E. J. Cairns,<sup>b,\*\*</sup> and F. McLarnon<sup>b,\*,z</sup>

<sup>a</sup>Materials Sciences Division, and <sup>b</sup>Environmental Energy Technologies Division,  
Lawrence Berkeley National Laboratory, University of California, Berkeley, California 94720, USA

A baseline cell chemistry was identified as a carbon anode,  $\text{LiNi}_{0.8}\text{Co}_{0.2}\text{O}_2$  cathode, and diethyl carbonate-ethylene carbonate  $\text{LiPF}_6$  electrolyte, and designed for high power applications. Nine 18650-size advanced technology development cells were tested under a variety of conditions. Selected diagnostic techniques such as synchrotron infrared microscopy, Raman spectroscopy, scanning electronic microscopy, atomic force microscopy, gas chromatography, etc., were used to characterize the anode, cathode, current collectors and electrolyte taken from these cells. The diagnostic results suggest that the four factors that contribute to the cell power loss are solid electrolyte interphase deterioration and nonuniformity on the anode; morphology changes, increase of impedance, and phase separation on the cathode; pitting corrosion on the cathode current collector; and decomposition of the  $\text{LiPF}_6$  salt in the electrolyte at elevated temperature.

© 2001 The Electrochemical Society. [DOI: 10.1149/1.1362541] All rights reserved.

Manuscript submitted May 15, 2000; revised manuscript received January 15, 2001.

Lithium-ion batteries are a fast-growing technology that is attractive for use in portable electronics and electric vehicles due to their relatively high specific energy and specific power. The Advanced Technology Development (ATD) Program is a new effort by the U.S. Department of Energy to aid the development of lithium-ion batteries for hybrid electric vehicle (HEV) applications.<sup>c</sup> A baseline cell chemistry was identified as a carbon anode (negative electrode), a  $\text{LiNi}_{0.8}\text{Co}_{0.2}\text{O}_2$  cathode (positive electrode), and diethyl carbonate (DEC)-ethylene carbonate (EC)-(DEC)-(EC)- $\text{LiPF}_6$  electrolyte. Various diagnostic techniques were applied to determine cell component chemical, structural, and morphological changes that lead to performance degradation and failure as they are aged, cycled and/or abused. These diagnostic results can be used to guide the improvement of cell chemistries.

Nine ATD baseline cells were fabricated by PolyStor, Inc. according to a design provided by ANL and tested at INEEL, ANL, and SNL. These cells were not optimized, and were used only in studies of cell components under high power battery simulations. High current pulse profiles were generated specifically for performance characterization of these batteries in HEV applications in contrast to the constant-current profiles typically used in the characterization of lithium-ion batteries for portable devices.<sup>1</sup> A cycle life testing profile for a charge-neutral 3% variation in cell state of charge ( $\Delta\text{SOC}$ ) is shown in Fig. 1.<sup>2</sup> Reference performance tests (RPT) were conducted at  $25 \pm 3^\circ\text{C}$  on all cells prior to testing and also periodically repeated during both calendar-life and life-cycle tests until an end-of-test criteria (see below) was reached. The RPT was performed every 4 weeks on cells that were held at 40, 50, and  $60^\circ\text{C}$  and every 2 weeks for cells tested at  $70^\circ\text{C}$ . The RPT included one C/1 constant-current discharge and one medium current hybrid pulse power characterization (HPPC) test, as well as impedance measurements at 100 and 0% SOC. The HPPC test is designed to assess battery performance by incorporating both discharge and regenerative pulses. Each single profile corresponds to 10% depth of discharge (DOD) at constant current at the 8C rate (7.2 A) (see the 2nd profile in Fig. 2), followed by a 1 h rest period to allow the cell to return to an equilibrium condition before applying the next profile. The end-of-test criterion is defined as the condition at which a

cell fails to perform the medium HPPC (8C) at 60% DOD within the discharge (3 V, see 3rd profile in Fig. 2) and regenerative voltage limits (4.1 V continuous and 4.3 V for up to a 2 s pulse). The power performance (W/kg) of all cells decayed by 15-30% during cycle-life and calendar-life testing. The cells were then discharged at the C/25 rate and stored at  $10^\circ\text{C}$ . Cells were opened (with care) in a helium atmosphere dry box, followed immediately by diagnostics.

There are many literature reports on evaluations of the performance of individual cell components in lithium-ion batteries.<sup>3</sup> Few reports, however, address the characterization of full sized lithium-

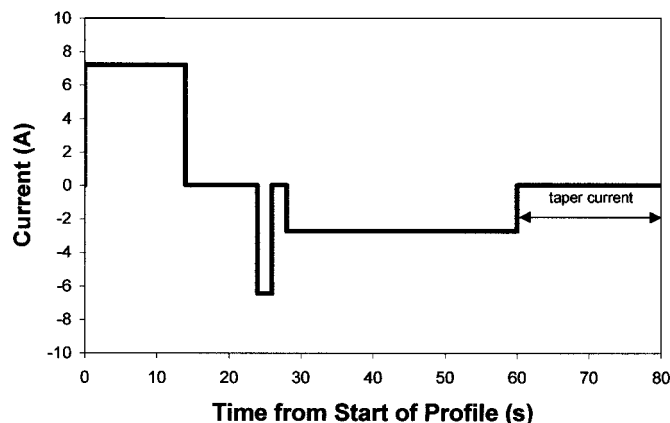


Figure 1. ATD cycle life testing pulse profile with  $\Delta\text{SOC}$  of 3% nominal.

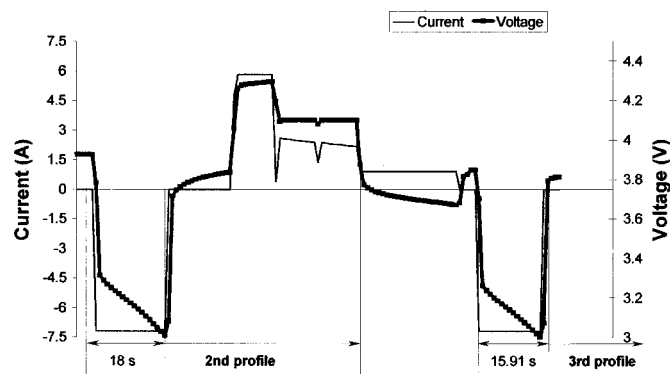


Figure 2. Medium current hybrid pulse power characterization test profiles.

<sup>c</sup> The ATD Program is a joint effort of five DOE National Laboratories: Argonne National Laboratory (ANL), Sandia National Laboratories (SNL), Idaho National Engineering and Environmental Laboratory (INEEL), Brookhaven National Laboratory (BNL), and the Lawrence Berkeley National Laboratory (LBNL).

\* Electrochemical Society Active Member.

\*\* Electrochemical Society Fellow.

<sup>z</sup> E-mail: fmclarnon@lbl.gov

Table I. ATD program generation 1 cell components.

Component	Anode	Cathode
Active material	75% MCMB graphite	84% $\text{LiNi}_{0.8}\text{Co}_{0.2}\text{O}_2$
Binder	17% SFG-6 carbon 8% polyvinylidene fluoride	Sumitomo 8% polyvinylidene fluoride
Additive	Kurecha C NA	Kurecha 1100 (homopolymer) 4% acetylene black, Shawinigan
Current collector	12 $\mu\text{m}$ Cu foil	4% graphite, SFG-6 20 $\mu\text{m}$ Al foil-uncoated
Loading (single-sided)	6.6 $\text{mg}/\text{cm}^2$	11 $\text{mg}/\text{cm}^2$
Separator	37 $\mu\text{m}$ three-layer (PE/PP/FE) from Celgard	
Electrolyte	1 M $\text{LiPF}_6$ in EC/DEC (1:1), LP-40 from EM Science (Merck)	

ion batteries.<sup>1</sup> Here, we report diagnostic results for techniques including synchrotron infrared (IR) microscopy, Raman spectroscopy, scanning electron microscopy (SEM), atomic force microscopy (AFM), gas chromatography (GC), cyclic voltammetry (CV), and electrochemical impedance spectroscopy on nine 18650-size ATD cells that were subjected to the test conditions described above.

### Experimental

**Chemicals.**—The cell characteristics are listed in Table I. Propylene oxide was obtained from Fluka with purity of 99.5%. Tetrahydrofuran (THF) was from J. T. Baker with  $\text{H}_2\text{O}$  content less than 0.003%. Both EC and DEC were purchased from Grant Chemical with less than 20 ppm of water.  $\text{LiClO}_4$  was obtained from EM industries. All chemicals were used as-received. Current collector strips were located at the ends of the anode (including the case of the battery), as well as at one-third and two-thirds of the distance along the length of the cathode. Cell 1, a so-called virgin cell, was subjected only to two formation cycles and one discharge at  $25 \pm 3^\circ\text{C}$ . Four cells (cell numbers 6 to 9) were subjected to life-cycle testing with 3 and 9% swings in their state of charge ( $\Delta\text{SOC}$ ) at 60 and 80% SOC, respectively. Calendar-life tests were performed on cell numbers 2 to 5 with these cells stored at various temperatures. A summary of the test conditions for all nine cells is given in Table II.

**Diagnostic techniques.**—*Ex situ* IR microscopy was conducted using a Nicolet Magna 760 with Nic-Plan IR microscope in the LBNL Advanced Light Source. A synchrotron beam was employed due to its high brightness and small spot size ( $\sim 10 \mu\text{m}$ ), which provides good spatial resolution and allows detailed examination of the uniformity of the solid electrolyte interphase (SEI) on electrodes. Airtight IR cells with KBr windows were constructed to perform IR microscopy on the air sensitive and moisture sensitive electrode materials. Electrode samples were harvested from various locations on the electrodes inside a dry box and then inserted into the IR cells. No other sample handling was performed, in order to preserve the electrode as it was in the battery. At minimum, three spectra were recorded for each sample to ensure that our results were reproducible. The same setup and reflectance geometry was employed for the IR measurements of electrolyte and other compounds such as propylene oxide on a glassy carbon substrate.

Model electrochemical experiments were carried out using glassy carbon as the working electrode and lithium metal as both counter and reference electrodes. The electrolyte used was LP40 (Merck, Inc) dissolved in THF at a 1:1 ratio, DEC/THF (1:1) or EC dissolved in THF with a concentration of 10  $\mu\text{M}$ , each with 0.1 M of  $\text{LiClO}_4$ . The potential was scanned from 2 V to 50 mV (vs.  $\text{Li}/\text{Li}^+$ ) at 20 mV/s, held for 5 min and subsequently brought back to 2 V.

*Ex situ* Raman spectra were recorded using a Coherent Inc. model Innova 70 argon ion laser,  $\lambda = 514.5 \text{ nm}$ , an HR320 Spec-

tograph (Instruments SA, Inc.), and an EG&G multichannel analyzer model 1463. The power of the incident laser beam ( $0.1 \times 3 \text{ mm}$ ) measured at the sample was 40 mW. Dry electrode samples were inserted into a hermetic spectroscopic cell in a He atmosphere glove box and then transferred to the spectrometer.

*Ex situ* atomic force microscopy (AFM) images were obtained with a Molecular Imaging scanning probe microscope coupled with a Park Scientific Instruments electronic controller. The AFM measurements were carried out in the constant force mode, *i.e.*, the piezoelectric scanner followed the surface contour of the sample and adjusted itself to the changing profile. AFM imaging was conducted in a small glove box specially designed for scanning-probe microscopy tests under a controlled  $\text{N}_2$  atmosphere. The samples were collected from the cathode  $\sim 2.5 \text{ cm}$  away from the current collector tab, washed in pure dimethyl carbonate (DMC), and stored in hermetic containers.

GC was used to analyze the components in the electrolyte. In a dry box, cell parts were cut from the separator, cathode, and anode for extraction and analysis by GC. The extraction technique used a specific sample size and solvent volume: 10 mL of methylene chloride (Burdick and Jackson HPLC grade) and 35 mg of separator (a 1.5 by 4 cm strip) followed by 2 h of extraction time reproducibly removed soluble compounds from the separator. This procedure could be performed in air or under He without observable differences in the chromatography results. Another extraction was employed using water and methylene chloride (Burdick and Jackson HPLC grade). The GC analysis was performed with an HP5890 series II instrument using a cryogenic cooling system and a flame ionization detector (FID). Each sample (5  $\mu\text{L}$  of methylene chloride) was on-column injected at  $-15^\circ\text{C}$  to minimize sample decomposition, and the column (DB-5) was heated to  $230^\circ\text{C}$  at  $10^\circ\text{C}/\text{min}$ . Control experiments were performed with standard compounds for retention time analysis and comparison. Control extractions and analysis confirmed that no soluble components were observed in the GC from the binder, carbon, cathode, current collector, or separator. Also, a sample of LP40 electrolyte was extracted as above, and the GC retention times for EC and DEC were identified as 11.9 and 8.7 min, respectively.

Thermogravimetric analysis (TGA, Perkin Elmer TGA 7) of  $\text{LiPF}_6$  (EM Sciences, reagent) was performed using an isothermal method under flowing nitrogen. A 20 mg sample of salt was loaded inside a dry box and transferred under He to the TGA sample holder, the sample was heated to  $70^\circ\text{C}$ , and the weight change was monitored over time. The procedure was repeated with a mixture of  $\text{LiPF}_6$  salt with nonvolatile polyethercarbonate polymer.

Controlled chemical reactions were performed to examine the reactivity of  $\text{PF}_5$  gas with electrolyte. Using a vacuum line, electrolyte components were exposed to  $\text{PF}_5$  gas and reacted at room temperature. The  $\text{PF}_5$  gas was generated by heating  $\text{LiPF}_6$  salt to  $70^\circ\text{C}$ , and was cold-trapped with the electrolyte (or solvent) in a liquid nitrogen bath. After the transfer, the reaction mixture was moved to

Table II. Test conditions of the ATD GEN-1 cells.

Cell no.	SOC	$\Delta$ SOC	Temp (°C)	Testing period (weeks)
1	0	0	20	0
2	80	0	40	4
3	60	0	50	12
4	80	0	60	4
5	60	0	70	2
6	60	3	40	4
7	60	3	70	2
8	60	9	40	4
	60	9	70	2

a dry box and warmed to room temperature. GC analyses of these reactions were performed as described above.

Electrochemical characterizations were performed on small samples ( $0.6 \text{ cm}^2$ ) of anodes and cathodes taken directly from the electrodes and studied electrochemically without any additional pre-treatment. Tests were performed in a helium atmosphere glove box without exposure to ambient conditions. Samples were weighed and assembled in stainless steel Swagelok cells with an  $0.5 \text{ mm}$  layer of lithium foil as the counter electrode and a thin lithium foil reference electrode sandwiched between two layers of Celgard 2400. The cell was flooded with about  $0.2 \text{ g}$  of LP40 electrolyte. Shorting between components was prevented by using a  $25 \text{ }\mu\text{m}$  polyethylene spacer with an  $0.6 \text{ cm}^2$  opening for the working electrode. Finally, a layer of thin exmet (Al for the cathode or Cu for the anode) was placed between the back side of the working electrode and the cell piston. This was necessary to assure good electronic contact through the unwetted back side of the dual-coated porous electrode. The exmet was compressed into the electrode to provide good contact to the current collector foil. CV was performed with a VMP multipotentiostat (BioLogic), and cell cycling was carried out with an Arbin battery cycler. Electrochemical impedance spectroscopy (EIS) measurements were carried out with a Solartron 1286 potentiostat and a Solartron 1260 frequency response analyzer, with a voltage perturbation of  $\pm 10 \text{ mV}$  after at least  $30 \text{ min}$  at open circuit. These measurements were recorded either as a function of time or state of charge, passing a fixed charge between measurements utilizing the batch mode of Zplot software. This automation was key to obtaining reproducible measurements with these electrodes.

An SEM (model ISI-DS130C) associated with an energy dispersive analysis by X-ray (EDAX) detecting unit was used to examine the surfaces of the current collectors. The adhesion between current collector and electrode material was generally good. For preparing appropriate current collector specimens for SEM observations, the top electrode materials were carefully removed by applying adhesive tape until a shiny surface was exposed.

### Results and Discussion

**Anode.**—Typical IR spectra from different anodes are shown in Fig. 3. The anode samples from the virgin cell (cell 1) were exposed to vacuum, and therefore, no bulk solvent from the electrolyte remained on the electrode surface. As expected, the spectrum shows essentially no peaks characteristic of the electrolyte. A broad peak at  $1650 \text{ cm}^{-1}$  was observed, which is characteristic of the C=O stretching of lithium alkylcarbonate, consistent with other literature reports.<sup>4</sup> The peak at  $838 \text{ cm}^{-1}$  is strong, and is a characteristic feature of the solid electrolyte interphase (SEI) as discussed later. A similar IR spectrum was obtained for cell 7 that was cycled at 60% SOC with a 3% SOC swing at  $70^\circ\text{C}$ , except that some electrolyte peaks were also observed because the sample was not evacuated. These results suggest that the SEI was formed during the formation cycles and remained even in cells that were subjected to 3%  $\Delta$ SOC at temperatures as high as  $70^\circ\text{C}$ . No significant signals from  $\text{Li}_2\text{CO}_3$  were observed in either IR or Raman measurements.

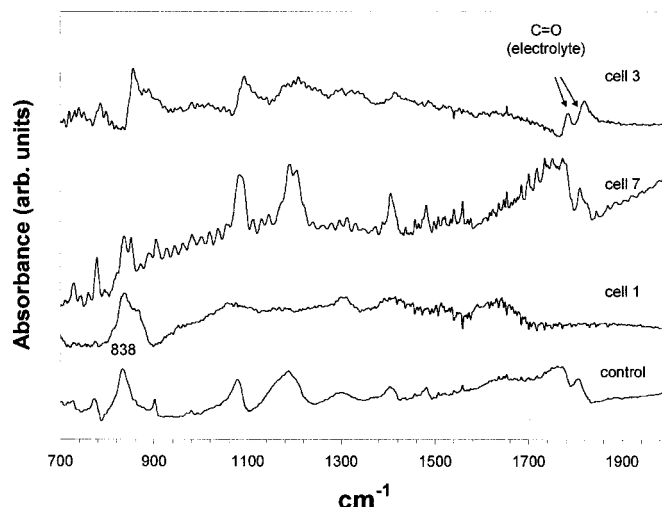


Figure 3. Typical IR spectra for the baseline ATD cell anodes with cell number indicated, and for the controlled electrochemical experiment of reduction of LP-40 on a glassy carbon electrode.

To understand the role that the solvent (DEC and EC) plays in the formation of the SEI, electrochemical control experiments were performed in DEC/THF- $\text{LiClO}_4$  and EC/THF- $\text{LiClO}_4$  electrolyte.  $\text{LiClO}_4$  was employed rather than  $\text{LiPF}_6$  due to its relative stability against reduction. No significant SEI was detected by IR when DEC was employed. EC was found to be the key contributor to SEI formation, as shown in Fig. 4b. The peak at  $838 \text{ cm}^{-1}$ , which was not seen in the electrolyte (Fig. 4a), was observed again and appeared to be most intense of all peaks observed. It was ascribed by Aurbach *et al.* to the bending mode of an organic carbonate group.<sup>5</sup> This SEI, however, shows a strong resemblance to propylene oxide (Fig. 4c), which also has an intense vibrational peak at  $838 \text{ cm}^{-1}$  arising from C-O-C stretching of the epoxide ring. It is known that EC can be synthesized using ethylene oxide and  $\text{CO}_2$ .<sup>6</sup> A mechanism for the reverse reaction, *i.e.*, EC decomposition to ethylene oxide or epoxide-containing material, however, is not available at this time.

The IR result was reproducible for each anode sample. Nonuniformity of the SEI layer was, however, observed for samples taken from different locations on anodes in tested cells. Only signals from the electrolyte were observed at some locations for a sample from cell 3 in the inner side close to the current collector. This result is likely due to spatial variations of current density. If so, more current collector strips could help to generate a more uniform SEI layer. The variation of pressure and temperature inside the cell could also play

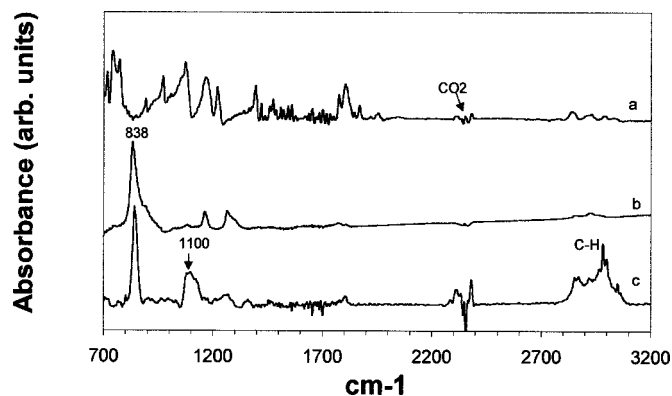
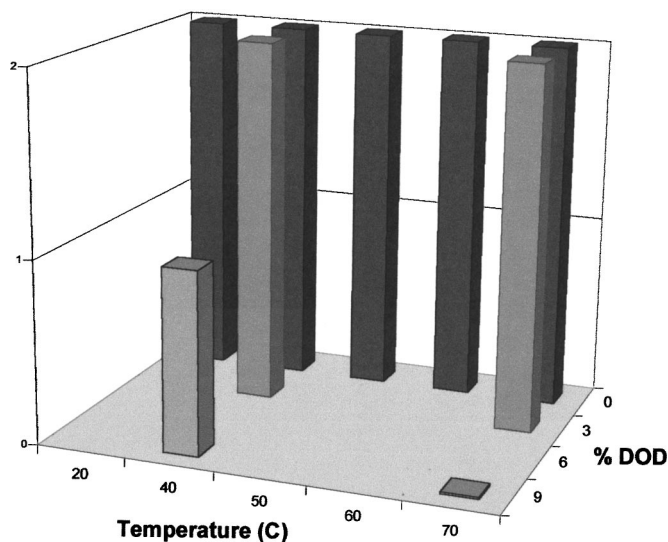


Figure 4. IR spectra for (a) the electrolyte EC/THF- $\text{LiClO}_4$ , (b) SEI from reduction of the electrolyte EC/THF- $\text{LiClO}_4$ , and (c) propylene oxide.



**Figure 5.** Qualitative analysis of SEI on anodes with temperature and  $\Delta$ SOC, with the bar height indicating the intensity of the peak at  $838\text{ cm}^{-1}$  being strong, weak, and none.

a role. Studies were carried out to investigate the cause(s) of this interesting phenomenon and its possible effects on cell performance.

LP40, diluted in THF in a ratio of 1:1, was reduced on a glassy carbon electrode. From both theoretical calculations performed at LBNL and reported in the literature,<sup>7</sup> THF should not be reduced on an inert electrode before lithium deposition. The resulting SEI on the glassy carbon electrode strongly resembles that on samples from the ATD cells. This encouraging finding shows that investigations of SEI layer formation in practical cells can be conducted using this simplified model system where a binder was not employed.

A qualitative trend analysis of SEI formation on anodes was carried out for these nine cells utilizing the peak at  $838\text{ cm}^{-1}$ , as shown in Fig. 5. This peak intensity is represented qualitatively by the relative heights of the bars as strong, weak and none and is plotted against both temperature and  $\Delta$ SOC. The effect of holding cells at 60% vs. 80% SOC was not considered in making this plot. Little change of the SEI layers is observed due to temperature variation alone and for cells that were cycled at 3%  $\Delta$ SOC. Cells that were cycled at 9%  $\Delta$ SOC, however, show a deteriorated SEI. IR spectroscopy detected no SEI remaining on the anode surface for cell 9, which was cycled in the most aggressive manner (9%  $\Delta$ SOC at  $70^\circ\text{C}$ ). Note that inorganic salts such as LiF are not IR sensitive. The work on electrolyte (later in this paper) suggests the possibility of LiF existence on the electrode surface in the form of a SEI that is not detected by IR spectroscopy.

Electrochemical characterization of the anodes was carried out using CV and EIS. In general, anode samples removed from the discharged cells showed an initial open circuit voltage (OCV) of 0.8 to 2.2 V against Li metal when reassembled in a Swagelok cell. The average sample weight was  $24\text{ mg/cm}^2$ . Capacity densities for a single side of the electrode were estimated from the weight, the thickness of the current collector foils, and the recipe for the electrode mix to be  $2.0\text{ mAh/cm}^2$ , assuming  $300\text{ mAh/g}$ . Cyclic voltammograms recorded with freshly assembled cells showed continuously increasing capacity and decreasing impedance with testing time. The first slow sweep CV recorded for anode samples from cells no. 1, 6, and 7 are shown in Fig. 6. The initial CVs show a trend of increasing peak separation, *i.e.*, a rise of impedance, with storage temperature. After CV cycling and three constant-current cycles with a taper charge between 0.01 and 1.0 V vs. Li, the capacity of the anode samples stabilized at  $\sim 2\text{ mAh/cm}^2$ , as expected for this electrode. A steady-state CV trace is also shown in Fig. 6. Similar CVs were recorded for all of the anode samples following

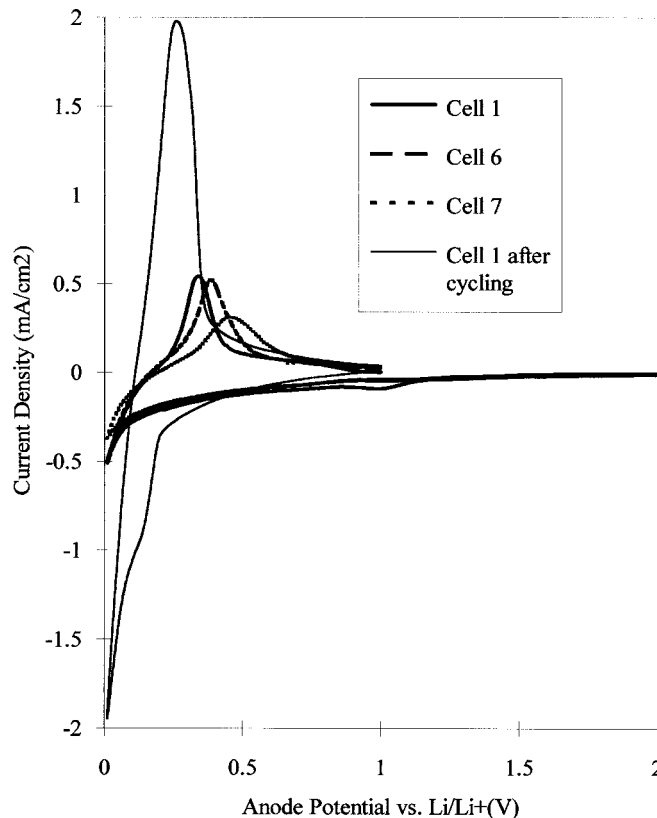


**Figure 6.** CVs for anode samples from cells tested/stored at three temperatures. Cell 1: formed only at  $25^\circ\text{C}$ ; cell 6: cycled at  $40^\circ\text{C}$ ; cell 7: cycled at  $70^\circ\text{C}$ .

this cycling protocol. The fact that this impedance decreases with cycling indicates possible formation of a resistive film or precipitates on the anode after removal of the volatile component (DEC) from the electrolyte. This layer then re-dissolves in the relatively large amount of electrolyte introduced in the Swagelok cells. The extent of formation of this resistive film appears to follow the trend of increasing with cell storage/test temperature. This film could be related to the epoxide peaks observed with Fourier transform infrared spectroscopy (FTIR) as discussed above. This point needs to be examined further.

**Cathode.**—Figure 7 shows topographic AFM images ( $23 \times 23\text{ }\mu\text{m}$  and  $5 \times 5\text{ }\mu\text{m}$  areas) of the cathode taken from cell 1 (Fig. 7a), and cell 7 (Fig. 7b) which was cycled at  $70^\circ\text{C}$  at 60% SOC and 3%  $\Delta$ SOC. The surface morphology of the fresh cathode can be described as formations of loosely packed  $\sim 10\text{ }\mu\text{m}$  particles of irregular shape, which are separated by deep intergranular crevices. The flattened grain surfaces were formed during the thin film calendaring which constituted part of the cathode manufacturing process. Close examination of the cathode surface at higher magnification reveals well-pronounced crystal planes and edges of individual grains of the active material.

Examination of the topographic AFM images of the cathode that was taken from the cell that was subjected to cycling at  $70^\circ\text{C}$  (Fig. 7b) reveals a significant change in the surface morphology. The initial large and flat grains of active material are still recognizable, but the entire surface is now covered by nanocrystalline deposits. The individual particle sizes varied from 50 to 200 nm. Considerable amounts of this deposit accumulated, particularly in the intergranular spaces. However, the nanoparticles can also be found scattered randomly across the crystal planes of the active material. Interestingly, we found a similar type of deposit on surfaces of almost all cathodes from cells that were subjected to either calendar-



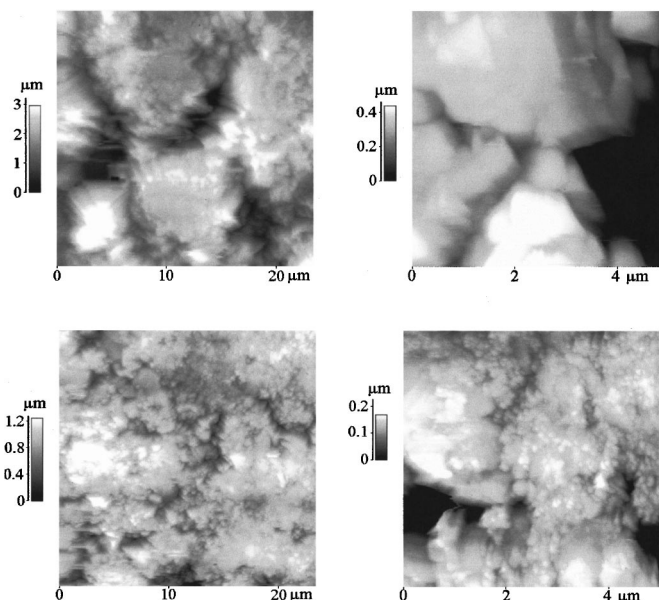


**Figure 7.** AFM topographic images of cathodes from the (a, top) cell 1, and (b, bottom) cell 7 (cycled at 70°C at 60% SOC and 3%  $\Delta$ SOC).

life or life-cycle tests. We determined that the amount of deposit and the extent of morphology modification depended on the test temperatures.

In order to quantify the AFM results and identify a clear relationship between the cathode surface morphology changes and the testing temperature, a statistical analysis of the AFM images was conducted. For every cathode, a series of AFM images was recorded at eight different locations and median values of surface-average roughness and root-mean-square (rms) roughness were calculated. Figure 8 shows the surface-average and rms roughness parameters expressed vs. temperature. The results at 20°C correspond to the uncycled cell 1. It is clear from Fig. 8 that both surface roughness parameters decrease monotonically with increasing temperature. This trend is consistent with visual observations from the AFM images. The smaller difference between the surface average and rms roughness values at higher temperatures suggests the formation of a more uniform surface with less protrusions and deep crevices. Interestingly, the smoothing effect was more pronounced in calendar-life cells compared to cycled cells. The nanocrystalline deposits, which accumulated preferentially in deep cavities between the grains of active material rather than on flat grain surfaces, contributed significantly to the smoothing effect. It is difficult to identify the specific mechanism of this smoothing effect based on our data. An electrochemical dissolution-deposition mechanism can be ruled out because we found similar deposits in calendar-life and cycled cells. Chemical dissolution of  $\text{LiNi}_{0.8}\text{Co}_{0.2}\text{O}_2$  and precipitation of reaction products from the electrolyte also appear to be unlikely. A plausible explanation for the observed phenomenon is cobalt and nickel oxide phase segregation, which may proceed via solid-state diffusion of  $\text{Ni}^{3+}$  and  $\text{Co}^{3+}$  ions. Another possible mechanism is the breakdown of large grains of  $\text{LiNi}_{0.8}\text{Co}_{0.2}\text{O}_2$  into smaller particles due to mechanical stress caused by a nonhomogeneous lithium distribution within large agglomerates of  $\text{LiNi}_x\text{Co}_{1-x}\text{O}_2$ .

To gain additional insight into the nature of the nanocrystalline deposit that forms at the cathode at higher temperatures, we studied the structure and composition of the cathode surface with Raman spectroscopy. Figure 9 shows Raman spectra of cathodes from cells 1 (Fig. 9a) and 3 (Fig. 9b). The Raman spectra of both cathodes are dominated by two strong and broad carbon bands at 1365 and 1580  $\text{cm}^{-1}$  and a broad maximum centered around 500  $\text{cm}^{-1}$ , characteristic for the  $\text{LiNi}_x\text{Co}_{1-x}\text{O}_2$  oxide. The large difference between the

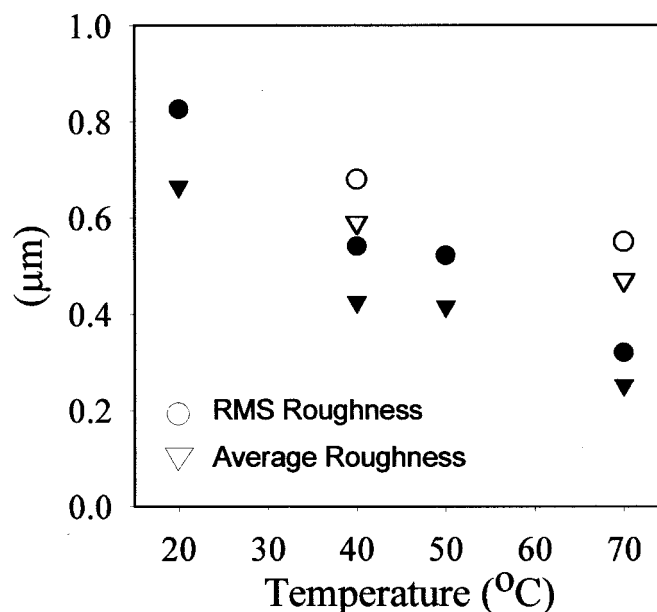


**Figure 8.** Calculated surface-average and rms roughness parameters of cathodes from the virgin cell (no. 1), calendar-life cells 2, 3, 5 (filled symbols) cycled cells 6 and 7 (open symbols) expressed vs. temperature.

band intensities is mainly due to the much larger Raman cross section of carbon compared to  $\text{LiNi}_x\text{Co}_{1-x}\text{O}_2$ , but is also due to a high concentration of carbon on the cathode surface. The  $\text{C}/\text{LiNi}_x\text{Co}_{1-x}\text{O}_2$  peak ratio varied significantly between locations, suggesting a nonuniform surface concentration of cathode components. These observations were also confirmed by electron spectroscopy for chemical analysis (ESCA) surface analysis.

The effect of cell testing on the cathode surface composition and structure becomes visible after close examination of the Raman bands that arise from  $\text{LiNi}_x\text{Co}_{1-x}\text{O}_2$ . The Raman spectrum shown in Fig. 9b, typical of those we recorded at random locations on almost all cathodes which were tested at higher temperatures, exhibits an intense peak at 558  $\text{cm}^{-1}$ . This band, along with the band at 480  $\text{cm}^{-1}$ , is usually associated with vibrations characteristic of Ni(III) and/or Ni(IV) oxides, and their presence can be detected in the spectrum of the virgin cathode. However, the rise of their intensities suggests selective dissolution of cobalt from the  $\text{LiNi}_x\text{Co}_{1-x}\text{O}_2$  or

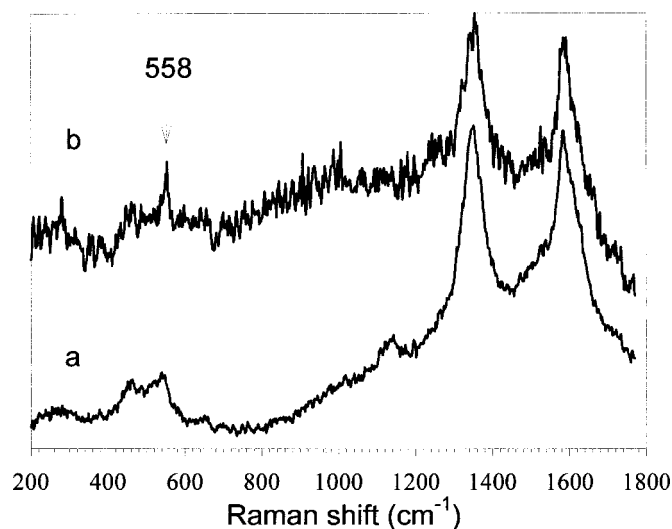


**Figure 9.** Raman spectra of cathodes from (a) cell 1, and (b) cell 3.

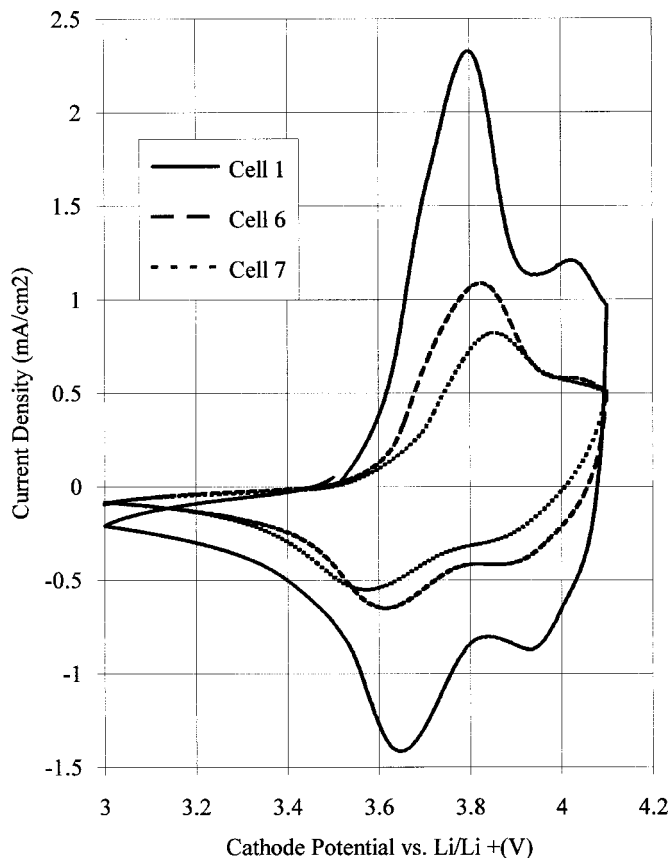


**Figure 10.** CVs for cathode samples from cells tested/stored at three temperatures. Cell 1: formed only at 25°C; cell 6: cycled at 40°C; and cell 7: cycled at 70°C.

the formation of a separate phase of nickel oxide at the cathode surface. The presence of a nanocrystalline deposit at the cathode surface supports this hypothesis. Mid-IR (wavenumber range 600-4000  $\text{cm}^{-1}$ ) data revealed no observable SEI layer on the cathode surface, which suggests that the precipitate does not arise from oxidation of the electrolyte.

Because nickel oxide is also active vs. lithium intercalation and deintercalation, it is difficult to evaluate how such surface material segregation could affect the electrode performance in this particular case. However, taking into account extensive electrode surface morphology modification which led to electrode decreased surface area and phase segregation in the relatively short testing time, we may assume that in the long term such surface changes can lead to significant electrode degradation and eventual failure. We do not expect such surface processes to decrease the bulk electrode capacity to a significant extent. However, the presence of a dense surface deposit consisting of separate phases of nickel and cobalt oxides may create an additional diffusion barrier for lithium ions and lead to increased electrode impedance.

The electrochemical performance of the cathodes was evaluated with small samples harvested from the cells and tested against lithium foil. Samples weighted an average of 32  $\text{mg}/\text{cm}^2$  with a theoretical capacity of 1.8  $\text{mAh}/\text{cm}^2$ , assuming 164  $\text{mAh}/\text{g}$  capacities for the active materials. Samples from cells disassembled in the discharged state (3.3 V) showed an OCV of 3.5 vs. lithium foil. Constant current cycling with a taper charge to 4.1 V was used to verify the capacity of the electrode samples. All samples tested showed close to the theoretical capacity indicating no discernible loss in bulk capacity as a function of test temperature or cycling history. Slow sweep voltammetry (0.1  $\text{mV}/\text{s}$ ) was also used to characterize the behavior of the cathode samples as shown for three cells

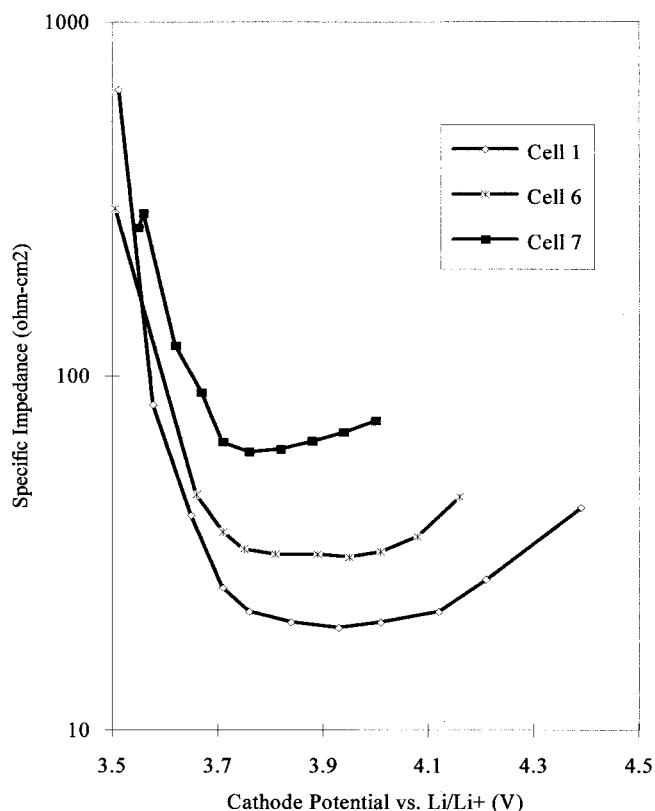


**Figure 11.** Specific impedance measurements at low frequency (100 mHz) for cathode samples from cells tested/stored at three temperatures. Cell 1: formed only at 25°C; cell 6: cycled at 40°C; and cell 7: cycled at 70°C.

in Fig. 10. The CV capacity recorded for the virgin cell cathode is very close to the theoretical value for one side of the electrode. The lower capacities reflected in Fig. 10 for the higher temperature cells reflects higher cathode impedance. This trend in the impedance of the cathode samples was characterized more completely with EIS. Analysis of the full spectra is beyond the scope of this paper. Instead, a single low-frequency (100 mHz) specific impedance is shown in Fig. 11 as a function of electrode SOC, as characterized by the electrode potential vs. lithium. There is a clear rise in cathode impedance at low SOC or high lithium content, consistent with literature results for these oxides. There is also a clear rise in impedance over the entire range of lithium content as a function of cell testing temperature. This could be directly related to the reduction in active material surface area in the cathode as observed with AFM results discussed above or the corrosion of the current collectors as discussed below.

**Current collectors.**—Electrochemical measurements described above revealed that the interfacial impedance (especially at the cathode) increases with temperature and contributes to the cell performance decline. The surfaces of current collectors from both the anode and cathode were examined via SEM. The surface of the Cu anode current collector showed only few cracks which might be related to the insufficient mechanical strength of thin foils. The Al cathode current collectors, however, showed extensive pitting corrosion. Figure 12 presents three typical SEM images of Al current collectors obtained from calendar-life cells tested at 20, 50, and 70°C (cells 1, 3, and 5). The pit number density is clearly correlated to testing temperature. Figure 13 shows that the pitting density doubled at elevated temperature, and that there is a clear break in behavior at 50°C.

It has been proposed that the highly oxidizing potential at the cathode is the primary factor that causes the surface corrosion of Al

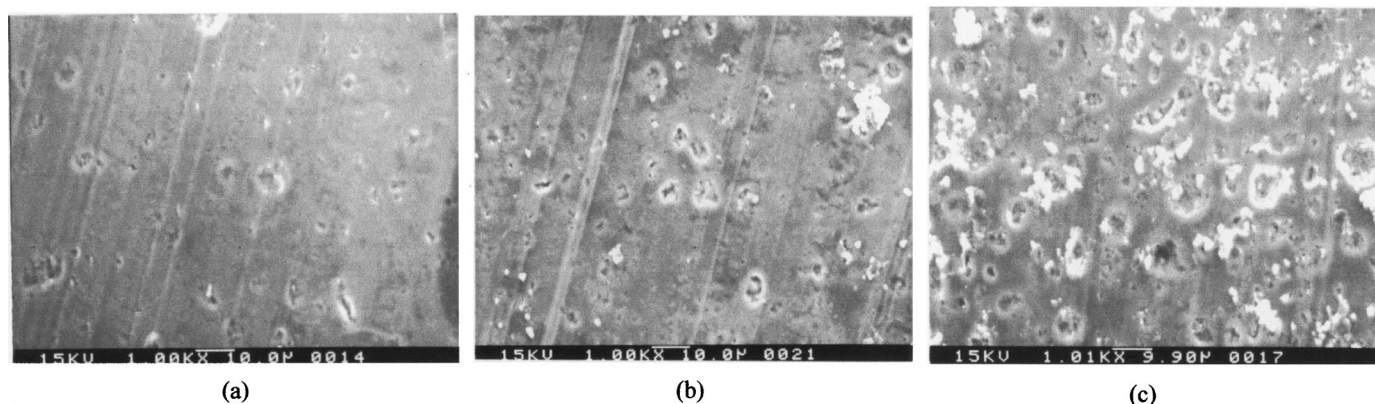


Figure 12. SEM of the Al current collectors from cells stored at various temperatures (°C) (a) 20, (b) 50, and (c) 70.

current collectors.<sup>8</sup> Our data show that pitting corrosion is present in both the calendar life cell, and the virgin cell. A pit number density as high as  $4.2 \times 10^3/\text{mm}^2$  was observed, with a 5% variation from sample to sample. The pit dimensions of  $\sim 10 \mu\text{m}$  are similar to the particle size of the cathode materials used. In addition, only Al, Fe (a trace amount), Ni, and Co (cathode constituents) were detected inside the corrosion pits. The corrosion phenomenon may be initiated by the surface damage when electrode material was laminated to the Al current collectors.

**Electrolyte.**—Our solvent extraction technique removed electrolyte components and new compounds (soluble, volatile components) from the cathode, anode, or separator. A GC trace (Fig. 14) from material extracted from the separator sample of cell 3 shows EC/DEC solvents as well as reaction products. These compounds and solvents were also observed in the anode and cathode, but only the anode contained ethylene glycol, which could be a product of the reaction of epoxide with water moisture in the air. This finding is consistent with the IR observation on the anode surface.

The reaction product at retention time 16.7 min diethyl-2,5-dioxahexane carboxylate (DEDOHC) was identified by comparison of its retention time with that of an authentic sample of DEDOHC. This compound derives from a transesterification reaction of EC and DEC. Close examination of the chromatogram shows the presence of less volatile products at longer retention times that are consistent with the formation of higher molecular weight oligomers that indicate the formation of polymers. More definitive analysis by GC/

Mössbauer spectroscopy, capillary electrophoresis, and high performance liquid chromatography is being undertaken to confirm the presence of polymers.

Comparing the peak area in the GC trace for the reaction product DEDOHC and that of EC provides quantitative information about the products created during cell testing. EC was chosen to serve as an internal standard due to its much lower volatility at room temperature. All of the cells tested in this study (except the virgin cell) exhibited nearly the same 0.13 ratio of DEDOHC:EC, except that significantly less DEDOHC was detected in the virgin cell.

$\text{LiPF}_6$  salt is not stable at elevated temperature. The isothermal TGA in Fig. 15 shows that a sample of  $\text{LiPF}_6$  loses 80% of its mass (likely to be  $\text{PF}_5$ ) after 200 min at  $70^\circ\text{C}$  under flowing nitrogen, then reaches a final value of 17% after heating to  $150^\circ\text{C}$ , indicating residual LiF. The reactive gas sublimates from solid  $\text{LiPF}_6$  salt in an equilibrium reaction that is sensitive to temperature. Decomposition can be described by the equilibrium equation

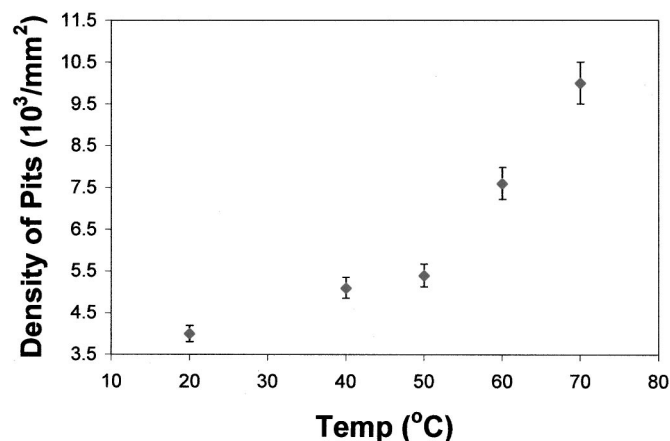
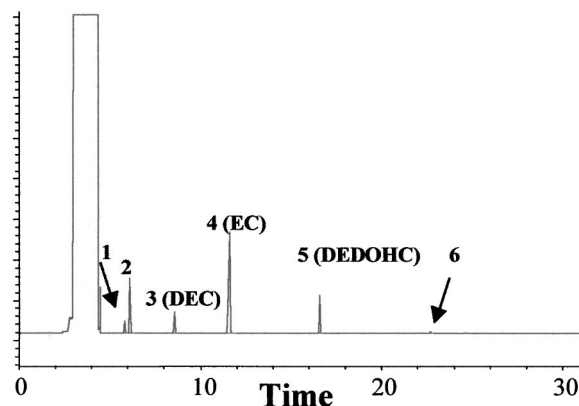


Figure 13. Correlation of pit number density on Al current collectors and cell temperature.



Pk#	Ret Time (Min)	Area %	Identification
1	5.85	2.8048	Reaction Product
2	6.15	11.3624	Reaction Product
3	8.61	3.6082	DEC
4	11.68	72.1361	EC
5	16.64	9.5739	DEDOHC
6	22.77	0.5146	Reaction Product

Figure 14. GC of the separator material harvested from cell 3. The cell was held at 60% SOC at  $50^\circ\text{C}$ .



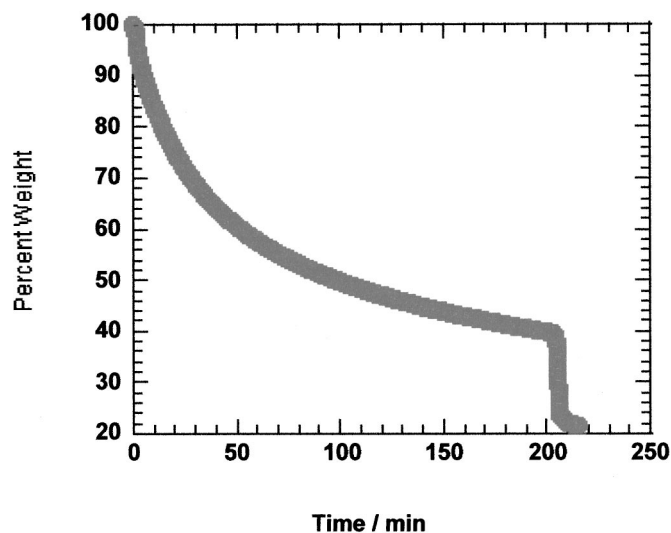


**Figure 15.** Percent weight of  $\text{LiPF}_6$  lost against time (minutes) during an isothermal TGA experiment at  $70^\circ\text{C}$  under flowing nitrogen.

Removal of  $\text{PF}_5$  gas by reaction or low vapor pressure forces the equilibrium to the product side. A similar but smaller weight loss is observed in the homogeneous, nonvolatile and viscous polymer electrolyte solution of  $\text{PolyCE}_3/\text{LiPF}_6$  ( $\text{CE}_3$  is bis-triethoxycarbonate) whereas no weight loss was observed for the mixture of  $\text{PolyCE}_3/\text{LiTFSI}$ .

To understand the reaction mechanism in these Li-ion cells which contain  $\text{LiPF}_6$ , a comparison between reactions of electrolyte components and  $\text{PF}_5$  gas was performed. The reactivity of  $\text{PF}_5$  gas and electrolyte components was apparent at room temperature: a mixture of  $\text{PF}_5$  and DEC produced a white precipitate and gas, but the solution remained clear. When 20 mL of LP40 electrolyte was exposed to 0.1 g of gas, after 10 h the electrolyte turned brown, produced gas, and precipitated a solid, a reaction that continued for 3 weeks (in a dry box) before stabilizing. We conclude that reactions involving EC are responsible for the insoluble brown product, furthermore, these reactions are likely responsible for the visible brown stain observed on each cell separator. The LP40 control reaction produced soluble components observable with GC, similar to those for the cell seen in Fig. 14, and the ratio of product DEDOHC to EC is similar to that in cells ( $\text{DEDOHC}:\text{EC} = 0.15$ ). Therefore, the reactions of LP40 and  $\text{PF}_5$  are expected to be responsible for the formation of DEDOHC both in the control reactions and in the ATD lithium ion cells.

Our electrolyte chemistry results are qualitatively consistent with general characteristics of cell failure by increasing cell resistance. Creation of  $\text{PF}_5$  contributes to cell performance decline:

1. Lost charge carriers due to  $\text{Li}^+$  entrapment in an insoluble salt,  $\text{LiF}$ ,
2. Increasing solvent viscosity due to the formation of oligomeric compounds from reaction between solvent and  $\text{PF}_5$ ,

3. Decreasing conductivity due to increasing solvent viscosity and charge carrier loss,

4. Increasing cell resistance that may be due to precipitation of polymer and insoluble salt on battery component surfaces. The increased resistances result in heat generation during charge and discharge and hence further salt decomposition that exacerbates cell power fade.

### Conclusions

An SEI is formed on the anode surface during cell formation cycles, and no changes were detected by IR for a cell that was cycled at 3%  $\Delta\text{SOC}$  and  $70^\circ\text{C}$ . The infrared spectroscopy of this surface layer showed a strong resemblance to that of propylene oxide. Nonuniformity of the SEI layer was, however, observed for samples taken from different locations on the anode in tested cells, which is likely due to spatial variations of current density. The SEI, however, deteriorated when cell was cycled at 9%  $\Delta\text{SOC}$  and at elevated temperature. The impedance of cathode samples increased monotonically with temperature, however, IR spectroscopy detected no SEI on the cathode surface. The impedance rise could be due to the change in morphology of the cathode surface with temperature observed with AFM or the increase in the density of pitting corrosion in the Al current collector observed with SEM. The electrolyte compositions were analyzed via GC, and ethylene glycol was identified as a reaction product from the anode, which is consistent with the IR observation of the epoxide-containing material.  $\text{LiPF}_6$  salt was found to be unstable at elevated temperature and could also contribute to the cell performance decline.

### Acknowledgments

This research was funded by the Assistant Secretary for Energy Efficiency and Renewable Energy, Office of Advanced Automotive Technologies, U.S. Department of Energy, under contract no. DE-AC03-76SF00098. The testing profiles for the ATD cells were kindly provided by INEEL. An authentic sample of DEDHOC was kindly provided by Dr. Khalil Amine of ANL. The authors gratefully acknowledge the tested cells, help and advice provided by the ATD program participants.

Lawrence Berkeley National Laboratory assisted in meeting the publication costs of this article.

### References

1. B. A. Johnson and R. E. White, *J. Power Sources*, **70**, 48 (1998).
2. ATD test plan for ATD 18650 GEN 1 lithium-ion cells, Revision 4, INEEL, Dec 8, 1999.
3. M. Winter, J. O. Besenhard, M. E. Spahr, and P. Novak, *Adv. Mater.*, **10**, 725 (1998).
4. D. Aurbach, Y. Ein-Eli, O. Chusid, Y. Carmeli, M. Babai, and H. Yamin, *J. Electrochem. Soc.*, **141**, 603 (1994).
5. D. Aurbach, M. L. Daroux, P. Faguy, and E. B. Yeager, *J. Electrochem. Soc.*, **134**, 1611 (1987); D. Aurbach, Y. Ein-Ely, and A. Zaban, *J. Electrochem. Soc.*, **141**, L1 (1994).
6. L. Vogdanis and W. Heitz, *Macromol. Rapid Commun.*, **7**, 543 (1986).
7. F. Paolucci, M. Carano, P. Ceroni, L. Mottier, and S. Roffia, *J. Electrochem. Soc.*, **146**, 3357 (1999).
8. J. W. Braithwaite, A. Gonzales, G. Nagasubramanian, S. J. Lucero, D. E. Peebles, J. A. Ohihausen, and W. R. Cieslak, *J. Electrochem. Soc.*, **146**, 448 (1999); Y. Chen, T. M. Devine, J. W. Evans, O. R. Monteiro, and I. G. Brown, *J. Electrochem. Soc.*, **146**, 1310 (1999).